Journal of Applied Physics

Dielectric tensor characterization and evaluation of several magneto-optical recording media

Cite as: Journal of Applied Physics **78**, 4076 (1995); https://doi.org/10.1063/1.359865
Submitted: 16 September 1994 . Accepted: 14 June 1995 . Published Online: 04 June 1998

Hong Fu, Zheng Yan, Seh Kwang Lee, and M. Mansuripur

View Online
Export Citation

ARTICLES YOU MAY BE INTERESTED IN

Magneto-optic Properties of Nickel, Iron, and Cobalt
Journal of Applied Physics **39**, 1276 (1968); https://doi.org/10.1063/1.1656263

Effective dielectric tensor for electromagnetic wave propagation in random media
Journal of Applied Physics **103**, 084901 (2008); https://doi.org/10.1063/1.2906135

Surface magneto-optic Kerr effect
Review of Scientific Instruments **71**, 1243 (2000); https://doi.org/10.1063/1.1150496

© 1995 American Institute of Physics.

Dielectric tensor characterization and evaluation of several magneto-optical recording media

Hong Fu,[a] Zheng Yan, Seh Kwang Lee,[b] and M. Mansuripur
Optical Sciences Center, University of Arizona, Tucson, Arizona 85721

(Received 16 September 1994; accepted for publication 14 June 1995)

We attempt to establish a dielectric tensor database for magneto-optical (MO) thin film materials with potential application for blue recording. For this purpose a method is developed for measuring the dielectric tensor of the MO layer within a multilayered stack. It uses a combination of ellipsometric, reflection/transmission, and polar MO Kerr effect measurements, and employs the MULTILAYER computer program to analyze the data. Using this approach we have measured the dielectric tensor for thin films of $BiDy_3(FeGa)_5O_{12}$ garnet, MnBi, multilayered Co/Pt, amorphous TbFeCoTa, and fcc cobalt in the wavelength range of 400–780 nm. The dielectric tensor for the Heusler alloy films of PtMnSb, which is available from the published literature, is also presented for the sake of completeness. These materials are then evaluated based on the intrinsic MO figure of merit defined by $\mathrm{FOM}\equiv|\epsilon_{xy}|/(2\,\mathrm{Im}\,\epsilon_{xx})$, where ϵ_{xx} and ϵ_{xy} are the diagonal and off-diagonal elements of the dielectric tensor of the MO material. In the blue–green regime of 400–550 nm, the relationship of the derived FOMs is as follows: $\mathrm{FOM}_{\mathrm{MnBi}}(\approx 0.027-0.045) \approx \mathrm{FOM}_{\mathrm{Garnet}}(\approx 0.023-0.032) > \mathrm{FOM}_{\mathrm{PtMnSb}}(\approx 0.015-0.026) > \mathrm{FOM}_{\mathrm{Co/Pt}}(\approx 0.013-0.015) \approx \mathrm{FOM}_{\mathrm{Co(fcc)}}(\approx 0.011-0.016) > \mathrm{FOM}_{\mathrm{TbFeCoTa}}(\approx 0.009-0.011)$. © *1995 American Institute of Physics.*

I. INTRODUCTION

As the magneto-optical (MO) recording technology continues to mature, the search for media with high MO performance at short wavelengths has become the focus of many research groups. The compilation of a database for the commonly used and potential MO materials is, therefore, timely at this point. In this paper we present the dielectric tensor for several MO media which are either used in commercial products or are being considered as candidates for the next generation devices that will operate with blue–green lasers. The dielectric tensor elements have been measured in the wavelength range of 400–780 nm, covering the full range of interest for both present and future MO data storage.

The dielectric tensor for an optically isotropic, perpendicularly magnetized MO thin film has the form

$$\epsilon=\begin{bmatrix} \epsilon_{xx} & \epsilon_{xy} & 0 \\ -\epsilon_{xy} & \epsilon_{xx} & 0 \\ 0 & 0 & \epsilon_{xx} \end{bmatrix}, \tag{1}$$

where XY is the plane of the film and Z is the normal direction. The dielectric tensor fully characterizes the optical and MO properties of the material, and is needed for designing the multilayers used in MO disks. Moreover, the maximum useful MO signal that can be obtained from any multilayer structure incorporating a given MO material is upper bounded by a quantity that depends solely on the dielectric tensor of the MO layer.[1] In the following we will briefly review this issue.

Consider a linearly polarized beam with the complex E-field amplitude E_x^{inc} that is normally incident on a sample of MO multilayer. Upon reflection the polarization state of the beam consists not only of an x component E_x^{ref}, but also of a y component E_y^{ref} that is produced by the MO effect. This phenomenon is described in compact form by the complex reflectivity matrix defined below:

$$\begin{pmatrix} E_x^{\mathrm{ref}} \\ E_y^{\mathrm{ref}} \end{pmatrix}=\begin{pmatrix} r_{xx} & r_{xy} \\ -r_{xy} & r_{xx} \end{pmatrix}\begin{pmatrix} E_x^{\mathrm{inc}} \\ 0 \end{pmatrix}. \tag{2}$$

The absolute value of the off-diagonal reflectivity $|r_{xy}|$, given by $|E_y^{\mathrm{ref}}/E_x^{\mathrm{inc}}|$, describes the efficiency of the sample in rotating the polarization. It turns out that $|r_{xy}|$ is also equal to the shot noise limited signal-to-noise ratio (SNR) in MO readout.[2] However, since $|r_{xy}|$ depends not only on the MO material but also on the multilayer stack in which the MO layer is embedded, it is not an adequate quantity for comparing different MO materials.

In Ref. 1 it is shown that, for a given MO material embedded in an arbitrary multilayer stack, the value of $|r_{xy}|$ is upper bounded by a figure of merit, FOM, which is solely determined by the dielectric tensor of the MO material:

$$\mathrm{FOM}=\frac{|\epsilon_{xy}|}{2\,\mathrm{Im}\,\epsilon_{xx}}. \tag{3}$$

Moreover, it is possible to design a quadrilayer structure for which $|r_{xy}|$ approaches the FOM in Eq. (3). The above FOM thus describes the intrinsic MO performance of the material, and as such, it provides a basis for the quantitative comparison of the performance of various MO materials.

The remainder of the paper is organized as follows: In Sec. II we describe the general measurement and computer analysis procedures by which the diagonal and off-diagonal tensor elements have been obtained. The dielectric tensor and the FOM for six materials of current interest are presented in Sec. III. Relevant measurement details and error analysis procedures are also described in this section. Section IV contains the concluding remarks.

[a]Present address: Komag Inc., 275 S. Hillview Dr., Milpitas, CA 95035.
[b]Visiting scientist from Materials Design Laboratory, Korean Institute of Sciences and Technology.

 0021-8979/95/78(6)/4076/15/$6.00 © 1995 American Institute of Physics

II. MEASUREMENT PROCEDURES AND DATA ANALYSIS

Our goal in this work is to determine the diagonal element ϵ_{xx} and the off-diagonal element ϵ_{xy} of the dielectric tensor of the MO layer. This MO layer may just be a single thin film on a substrate, or it may be embedded in a multilayer structure. To achieve this goal, one must measure the thicknesses and optical constants of all the layers within the multilayer stack. This usually requires elaborate measurements and sophisticated data analysis. Several techniques have been developed for this purpose.[3–5] Reference 3 describes an approach in which the ordinary optical constants of the MO film are obtained from the substrate–metal interface by ellipsometric measurements through a Dove prism, and the MO constants are obtained from the Kerr effect measurements through the dielectric coating–metal interface on the opposite side of the sample. This method requires the absorbing MO layer to be thick enough to prevent the occurrence of multiple reflections within the layer, and also requires accurate information regarding the optical constants and thickness of the overcoating layer. These requirements place strong limitations on the applicability of this method. The approach introduced in Ref. 4 employs a custom-made variable angle ellipsometer capable of measuring seven curves of reflectivity versus angle of incidence under different conditions of polarization and applied magnetic field. Again there are limits to the complexity of the multilayer stack that can be analyzed with this method. The method used in this present paper consists of ellipsometric measurements, normal reflectance and transmittance measurements, polar MO Kerr effect measurements, and, especially, data analysis using the MULTILAYER computer program.[16]

We used three instruments in our measurements. One is a multiwavelength variable-angle ellipsometer (MWVAE).[7] This ellipsometer uses a mercury lamp as the light source; different wavelengths in the range of 360 nm$\leqslant\lambda\leqslant$860 nm can be selected by using 1 of the 14 available filters. The bandwidth $\Delta\lambda$ (full width at half-maximum) of the filters is about 10 nm, yielding a coherence length ($=0.5\ \lambda^2/\Delta\lambda$) on the order of 10 μm, which is much larger than any film thickness of our samples. This allows the treatment of the probe beam as a coherent, monochromatic plane wave in data analysis. The angle of incidence Θ_{inc} in MWVAE is adjustable within the range of $35°\leqslant\Theta_{inc}\leqslant 80°$, with an accuracy better than 0.02°. We use MWVAE to shine linearly polarized light on the sample and measure the rotation angle θ and the ellipticity angle ϵ of the reflected beam. These angles are illustrated in Fig. 1, where Θ_{inc} is the angle of incidence, Ψ_{pol} is the polarization angle of the incident beam as measured from the p direction, θ is the rotation angle (i.e., difference between the orientation angle of the major axis of the reflected polarization ellipse and Ψ_{pol}), and ϵ is the ellipticity angle of the reflected polarization ellipse. The ellipticity is positive (negative) if the sense of rotation of the E field is clockwise (counterclockwise) when the beam propagates towards the observer. By rotating the quarter-wave plate (QWP) and the analyzer in the detector arm of the ellipsometer, one can extinguish the light at the detector and obtain

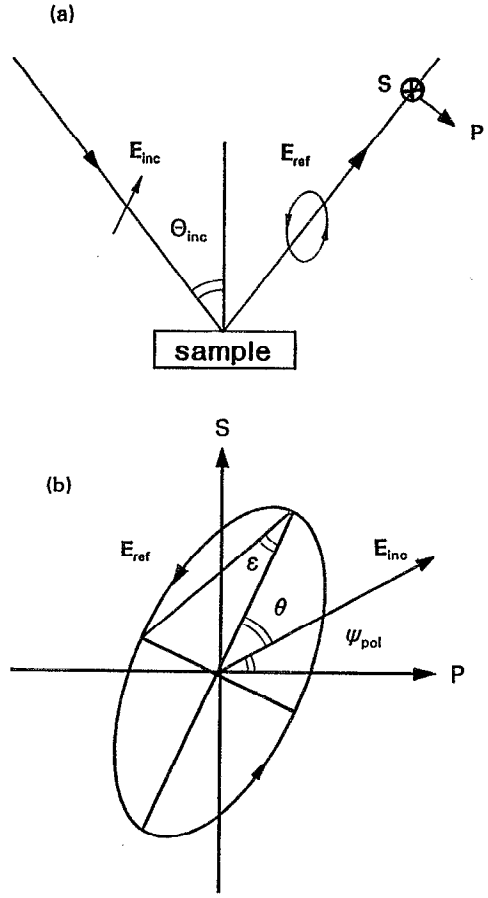

FIG. 1. (a) Schematic diagram corresponding to our ellipsometric measurement with MWVAE. The incident beam is linearly polarized, while the reflected beam is elliptically polarized. (b) The polarization ellipse is characterized by the rotation θ and the ellipticity ϵ. These angles are measured in the range of $35°\leqslant\Theta_{inc}\leqslant 80°$ for a fixed value of Ψ_{pol} at each λ.

the values of θ and ϵ. The accuracy of measuring θ and ϵ in our instrument is usually better than 0.05°.

The second instrument used in our work is a custom-made MO Kerr spectrometer (the MOKS system),[8,9] which allows the measurement of the Kerr rotation angle θ_k, Kerr ellipticity angle ϵ_k, normal reflectance R, and normal transmittance T, all as functions of λ in the range of 360 nm$\leqslant\lambda\leqslant$1050 nm. For samples with $R\geqslant 0.2$, the measurement accuracy for θ_k and ϵ_k is better than 0.01°. The accuracy for measuring R and T is better than ± 0.005. We also used an MO loop tracer[10] to measure the Kerr hysteresis loop for each sample at $\lambda=633$ nm. The hysteresis loop shows the orientation of the magnetization within the sample (in-plane or perpendicular), and also provides the values of the saturation field H_s and the coercive field H_c, from which we determine the magnetic field necessary for maintaining perpendicular magnetization during the measurement of θ_k and ϵ_k.

We measure four sets of data at each wavelength: **set 1**: rotation θ and ellipticity ϵ versus Θ_{inc} for linearly polarized incident beam (using MWVAE); **set 2**: reflectance R at normal incidence (MOKS); **set 3**: transmittance T at normal incidence (MOKS, only for transparent or semitransparent samples); **set 4**: Kerr rotation θ_k and ellipticity ϵ_k at normal incidence (MOKS). The first three sets of data are used to

determine the thickness D and the diagonal element ϵ_{xx} (or n and k as defined by $n + ik = \sqrt{\epsilon_{xx}}$) of the various layers. Data set 4 is used to determine the off-diagonal element ϵ_{xy}.

The data of θ and ϵ versus $\Theta_{\rm inc}$ measured at different wavelengths provide the essential information for determining the thickness D and the values of n and k. To obtain the most reliable and informative measurement data, consideration has to be given to several aspects of the measurements. One of them is the choice of a proper polarization angle for the incident beam. At any given $\Theta_{\rm inc}$, the values of (θ, ϵ) depend on the value of $\Psi_{\rm pol}$ and the multilayer's complex reflectivities $r_p=|r_p|\exp(i\phi_p)$ and $r_s=|r_s|\exp(i\phi_s)$, corresponding to the p- and s-polarized incident beams. The relevant relations are[2]

$$\tan[2(\Psi_{\rm pol}+\theta)]=\frac{2|r_s/r_p|\tan\Psi_{\rm pol}}{1-|r_s/r_p|^2\tan^2\Psi_{\rm pol}}\cos(\phi_s-\phi_p) \tag{4}$$

and

$$\sin(2\epsilon)=-\frac{2|r_s/r_p|\tan\Psi_{\rm pol}}{1+|r_s/r_p|^2\tan^2\Psi_{\rm pol}}\sin(\phi_s-\phi_p). \tag{5}$$

Equations (4) and (5) show that, in cases where $|r_s/r_p|\tan\Psi_{\rm pol}=0$ or 1 or $\gg 1$, we will lose information from either ϵ or θ or both. These extreme cases should, therefore, be avoided. Our experience shows that $\Psi_{\rm pol}$ should be fixed at such a value that $|\epsilon|$ in the entire range of $\Theta_{\rm inc}$ would fall within the range of several degrees, up to about 20°. We usually choose $\Psi_{\rm pol}=20°$ or 30° for transparent samples, and $\Psi_{\rm pol}=60°$ for metallic samples. Equations (4) and (5) also show that, for small phase difference $(\phi_s-\phi_p)$, which is common for many samples, only ϵ contains first order information on $(\phi_s-\phi_p)$. This is why in many cases the values of the film thickness D and absorption coefficient k depend sensitively on ϵ.

It is important that θ and ϵ be measured in the entire range of $35°\leqslant\Theta_{\rm inc}\leqslant 80°$. This reduces the influence of random errors of measurement, and also provides more information about the sample when more than two unknowns are involved. More importantly θ and ϵ may be insensitive to certain unknown parameters at some $\Theta_{\rm inc}$, where a small error in θ and ϵ could cause large errors in the final results. For example, for one of our single layer samples with known thickness (see Sec. III D), we compared the values of n and k estimated from the entire curves of θ and ϵ $(35°\leqslant\Theta_{\rm inc}\leqslant 80°)$ with those obtained from only a few points $(35°\leqslant\Theta_{\rm inc}\leqslant 40°)$. We found essentially the same value for n in both cases, but the difference in the k values was over 20%. In this case, the interference of the two beams returning from the front facet of the film and from its interface with the substrate obscures the effects caused by k at small incident angles. Consequently, θ and ϵ in the small angle range do not depend sensitively on the value of k.

The sign of ϵ is also an important factor in determining the multilayer parameters. To determine the sign of ϵ we must distinguish the fast axis of the QWP from its slow axis, and also distinguish the major and minor axes of the polarization ellipse of the reflected beam. (For thick, monolayer absorbing films the sign of ϵ is not critical, since the wrong sign usually leads to some nonphysical result, such as a negative absorption coefficient.) To eliminate spurious reflections from the bottom side of a transparent substrate, we always cover the bottom of the substrate with a black tape. We verified experimentally that, in the case of samples containing an MO layer, the effects of the magneto-optical rotation and ellipticity on the estimated values of n and k are negligible. We also verified that the optical anisotropy in our samples (if there is any) is negligible.

The reflectance R and transmittance T versus λ (data sets 2 and 3) are measured at normal incidence with MOKS. The reflectance is complementary to set 1 in the sense that here we measure the total reflected power, but not the ratio of s and p components. For some samples, the profile of R versus λ shows peaks and valleys caused by interference, which is helpful in estimating the thickness range of the layer responsible for such behavior. Transmittance gives another constraint on the acceptable values of D, n, and k, which is particularly valuable in the case of small k (say $k<0.1$). Sometimes there exist more than one set of parameters that give good fits to the rotation and ellipticity data versus $\Theta_{\rm inc}$. In these cases the reflectance and transmittance data are necessary (and usually sufficient) to remove the ambiguity.

The Kerr rotation θ_k and ellipticity ϵ_k are used to obtain the off-diagonal tensor element $\epsilon_{xy}[\equiv|\epsilon_{xy}|\exp(i\phi)]$ of the MO layer. The numerical calculations show that the signs of ϵ_k and θ_k do not affect the value of $|\epsilon_{xy}|$, but they do affect the value of ϕ. Therefore, attention has to be paid to measuring the correct sign for these angles. Using the measured R, θ_k, and ϵ_k, we can calculate $|r_{xy}|$ from the following formula:[2]

$$|r_{xy}|\simeq\sqrt{R(\theta_k^2+\epsilon_k^2)}, \tag{6}$$

where θ_k and ϵ_k are in radians. For each of our samples, we will compare $|r_{xy}|$, which is the figure of merit for that particular sample, with the FOM of Eq. (3), which is the figure of merit for the MO material incorporated in that sample.

The MULTILAYER[6] program has been used to analyze the measurement data. This program solves Maxwell's equations for a plane wave incident on a multilayered stack, and computes θ, ϵ, R, T, θ_k, ϵ_k, and other properties of the reflected and transmitted beams. The unknown parameters of the multilayer stack can be obtained by searching for the best match between theory and experiment. The quantity that is minimized in searching for the unknown parameters is the root-mean-square error $\mathscr{E}_{\rm rms}$ between the theoretically calculated and the measured data. In matching the rotation θ and the ellipticity ϵ, for example, $\mathscr{E}_{\rm rms}$ is given by

$$\mathscr{E}_{\rm rms}=\sqrt{\frac{1}{N}\sum_{i=1}^{N}[(\theta_i^{\rm thry}-\theta_i^{\rm expt})^2+(\epsilon_i^{\rm thry}-\epsilon_i^{\rm expt})^2]}, \tag{7}$$

where thry indicates the calculated value using the MULTILAYER program, expt stands for the experimental data, and the summation is over, for example, data points taken at different angles of incidence.

We first fit the sets 1, 2, and 3 of the measurement data taken at all wavelengths to determine the best-estimate values of D and ϵ_{xx} for each layer. This is done in the same

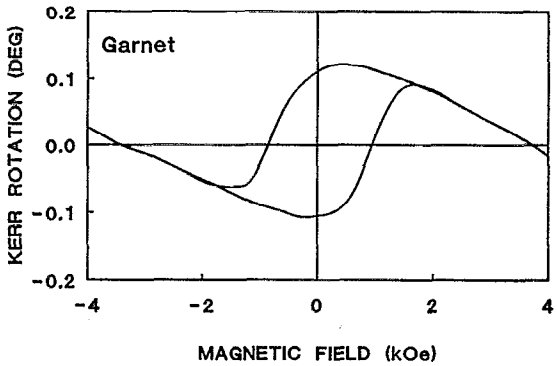

FIG. 2. Kerr hysteresis loop for the garnet sample at $\lambda=633$ nm. In the measurement the film side was coated with aluminum and the light was incident from the substrate. The loop is inclined towards the horizontal axis due to the paramagnetism of the GGG substrate.

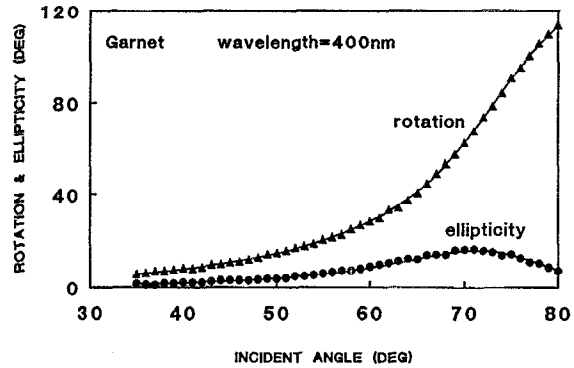

FIG. 3. Measured θ (triangles) and ϵ (circles) vs Θ_{inc}, and the best match (solid curves) at $\lambda=400$ nm for the BiFe garnet sample. The incident polarization angle $\Psi_{pol}=20°$.

computer run, in which ϵ_{xx} is independently adjusted for each wavelength, while D is kept constant for all the wavelengths. Certain details of this procedure, especially those leading to the best-estimate value of D, will be described in Sec. III A. The off-diagonal element ϵ_{xy} for the MO layer can be readily obtained once D and ϵ_{xx} for each layer have been determined. In this case, we keep the D's and ϵ_{xx}'s constant, and only adjust ϵ_{xy} of the MO layer in the MULTILAYER program to fit the measured values of θ_k and ϵ_k. The fitting process converges rapidly and always gives a unique solution for ϵ_{xy}.

TABLE I. Best-estimate values of refractive indices, dielectric tensor elements, and thickness for the sample of $BiDy_3(FeGa)_5O_{12}$/GGG substrate.

Layer material thickness Wavelength (nm)	Layer 1 $(BiDy)_3(FeGa)_5O_{12}$ 113 nm				Substrate $Gd_3Ga_5O_{12}$ (GGG) 0.45 mm	
	n	k	ϵ_{xx}	ϵ_{xy}	n	$k\times10^5$
360	2.586	0.638	6.26 $+i3.34$	0.096 $-i0.018$	2.121	2.0
400	2.769	0.469	7.44 $+i2.65$	-0.029 $i0.152$	2.053	0.8
450	2.662	0.306	6.99 $+i1.66$	-0.060 $i0.055$	2.002	0.5
500	2.644	0.129	6.97 $+i0.88$	-0.046 $+i0.014$	1.977	0.4
550	2.256	0	4.65	0.065 $-i0.006$	1.966	0.3
600	2.287	0	5.23	0.019 $-i0.024$	1.960	0.2
633	2.322	0	5.39	0.015 $-i0.004$	1.958	0.1
650	2.297	0	5.28	0.005 $+i0.004$	1.955	0.0
700	2.351	0	5.53	0.002 $-i0.001$	1.949	0.0
750	2.323	0	5.40	0.004 $+i0.002$	1.942	0.0
780	2.318	0	5.37	0.004 $+i0.002$	1.938	0.0

III. MEASUREMENT RESULTS

A. $(BiDy)_3(FeGa)_5O_{12}$ garnet

Bi-substituted polycrystalline garnet films have attracted much attention as potential candidate materials for future generations of high density magneto-optical recording media in the range of 400 nm$\leq\lambda\leq$500 nm.[11–13] Our sample consists of 10 bilayers of $(BiDy)_3(FeGa)_5O_{12}$ garnet, 95 Å thick, and cobalt, 5 Å thick, sputtered on a substrate of $Gd_3Ga_5O_{12}$ garnet (GGG), and crystallized under conditions of rapid thermal annealing. The nominal film thickness is 100 nm. We will treat the garnet layer as a single layer in the data analysis. In order to obtain appreciable Kerr rotation for the hysteresis loop, we coated one piece of the sample with aluminum and measured the Kerr rotation through the substrate side. The hysteresis loop (see Fig. 2) shows that the sample has perpendicular magnetic anisotropy, and its coercivity H_c is about 1 kOe.

To achieve higher measurement accuracy for the garnet film, we first measured n and k for the bare GGG substrate. Since the substrate is thick but transparent, k must be very small, and may be neglected in the measurement of n. We measured θ of the reflected beam at $\Theta_{inc}=80°$ for $\Psi_{pol}=30°$. At this incident angle both p and s components of the reflected beam are large and θ can be measured accurately. This method is better than measuring the Brewster's angle Θ_B, because near Θ_B the reflected intensity of the p beam is proportional to $(\Theta_{inc}-\Theta_B)^2$, and is so weak over a range of Θ_{inc} that the signal is blurred by the fluctuations of background light. To determine k, we measured the transmittance T of the bare substrate at normal incidence. Taking into account the reflection losses at both surfaces of the substrate, we have

$$T=\frac{16n^2}{(1+n)^4}\exp\left[-\frac{4\pi kd}{\lambda_0}\right], \tag{8}$$

from which we determined the values of k at different λ ($d=0.45$ mm is the thickness of the GGG substrate). The values of n and k are listed in Table I, and will be used later on in the data analysis for the original sample of BiFe garnet film.

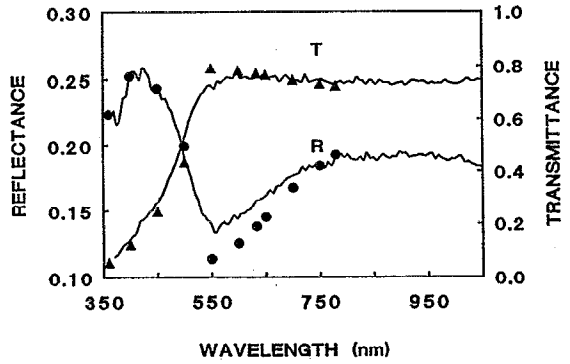

FIG. 4. Measured reflectance R (front surface) and transmittance T vs wavelength λ for the BiFe garnet sample (continuous curves). The circles and triangles are the calculated values using best-estimate parameters.

All four sets of data were measured for the sample of BiFe garnet. We measured θ and ϵ in 1° steps within the range of $35° \leq \Theta_{inc} \leq 80°$, at λ=360, 400, 450, 500, 550, 600, 650, 700, 750, and 780 nm. Figure 3 shows the measured θ and ϵ versus Θ_{inc}, and the best fit curves generated by the MULTILAYER program for λ=400 nm. At most wavelengths ϵ reaches its maximum value around Θ_{inc}=70°, implying that the reflected p and s beams acquire the largest phase difference. This is one of the reasons why we measure θ and ϵ for the largest possible range of Θ_{inc}.

Figure 4 shows the measured R and T versus λ, along with the calculated values using the best-estimate parameters. The average mismatch for R is less than 0.02, and that for T is less than 0.01. It should be noticed that the best-estimate parameters are obtained by matching all three sets of measurement data, namely, θ and ϵ versus Θ_{inc}, as well as R and T at normal incidence. Since the ellipsometric data (θ, ϵ) are measured within a larger range of incident angles and with higher accuracy, we have chosen the weight factors in the matching process such that the best-estimate parameters are primarily determined by the ellipsometric data. Aside from measurement errors in R and T, we believe that most of the mismatch between the calculated (R,T) and the measured (R,T) is due to the nonuniformity of the sample throughout its thickness.

Perhaps the most challenging part of the data analysis process is determining the thickness for the BiFe garnet film. The difficulty lies in the fact that it is not easy to separate the effects of k and D on the phase of the probe beam. Specifically, when matching the measurement data for a given wavelength, we found that, if we search for n, k, and D simultaneously, then the estimated set of parameters (n, k,

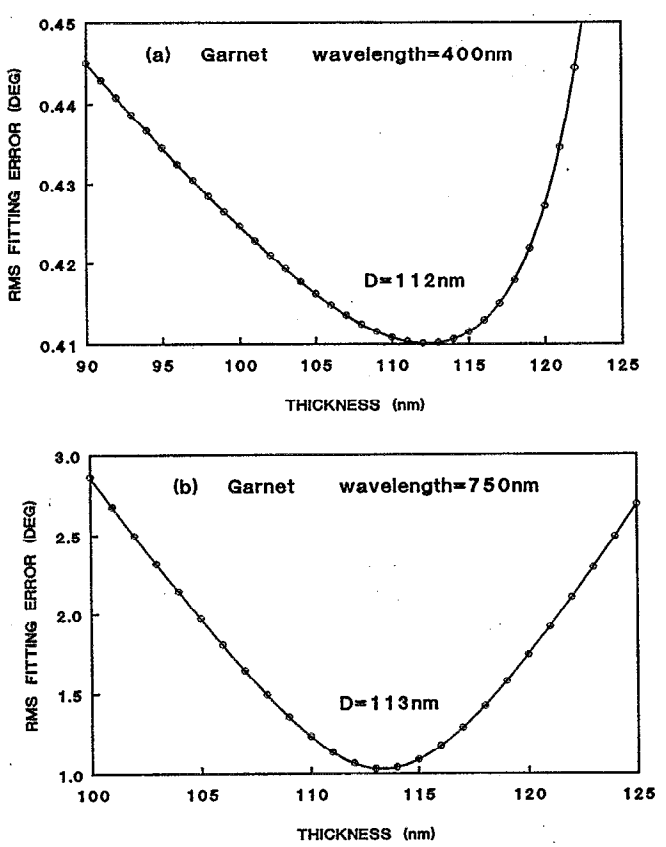

FIG. 5. The rms fitting error $\mathscr{E}_{rms}$ vs the assumed film thickness D. The measured data used in the calculations were taken at (a) λ=400 nm, which gives the best-estimate thickness D=112 nm, and (b) λ=750 nm, which gives the best-estimate D=113 nm.

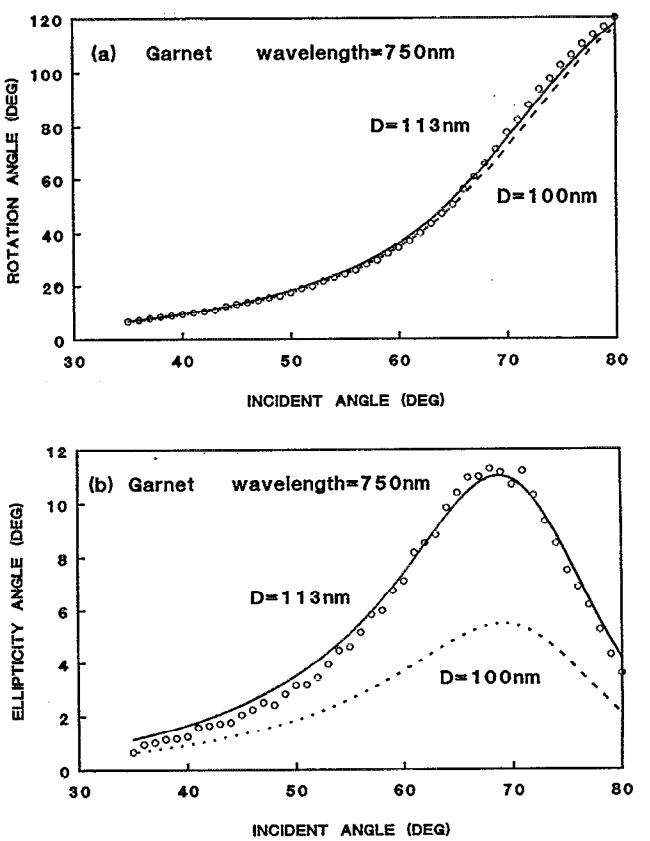

FIG. 6. Comparison of fitting quality for θ (a) and ϵ (b) using different values of the assumed thickness. The measured data (circles) are taken at λ=750 nm. The solid curves are the best fits calculated with D=113 nm, while the dashed curves are the fits obtained with the nominal thickness D=100 nm. (In both fitting processes the values of n and k are adjusted for minimum error.)

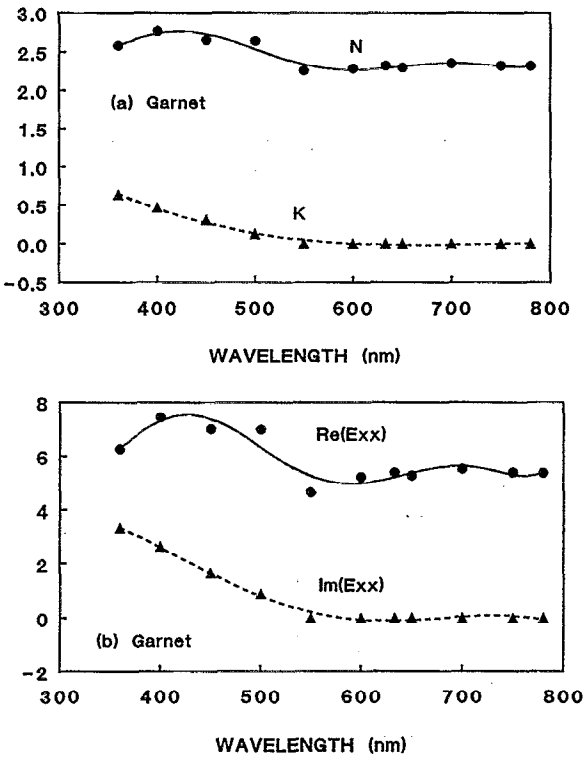

FIG. 7. (a) Plots of n and k for the BiFe garnet vs λ. (b) Plots of the real and imaginary parts of ϵ_{xx} for the BiFe garnet vs λ.

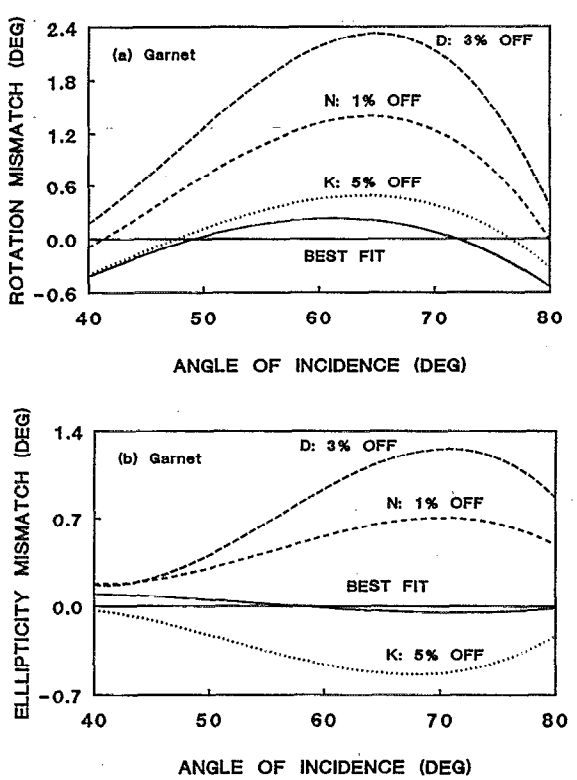

FIG. 8. Mismatch between calculated and measured values of θ (a) and ϵ (b) for different sets of parameters. The measured θ and ϵ were taken at λ=500 nm. A perfect match to the measured data would have produced the straight lines at zero. The solid curves represent the best-estimate values of the parameters. The short-dashed, the long-dashed, and the dotted curves are calculated by changing one of the three best-estimate parameters n, k, and D by the indicated amount.

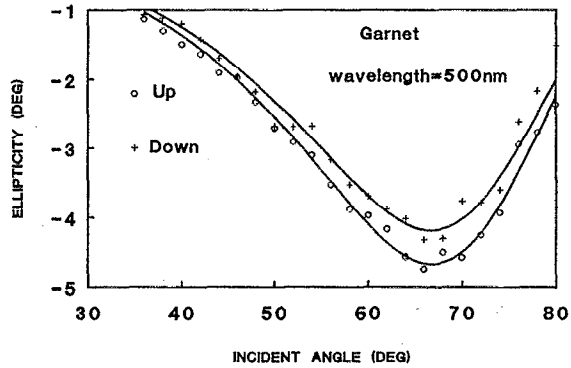

FIG. 9. Measured ϵ (circles: up magnetization; plus signs: down magnetization) and the best match (continuous curves) vs Θ_{inc} for opposite magnetization directions of the BiFe garnet sample. The data were measured with $\Psi_{pol}=20°$ at λ=500 nm. The error caused by the Kerr effect is <0.2% for the estimated value of n, <6% for the estimated value of k, and <1% for the estimated value of D.

D) is not unique, and quite often the estimated value of D depends on the chosen initial value. On the other hand, we found that, for a fixed value of D, the estimated values of (n, k) are unique, as is the fitting error $\mathscr{E}_{rms}$. This observation suggests that, in order to obtain the best-estimate value of D, we should first search for the minimum of $\mathscr{E}_{rms}$ for given D by adjusting n and k. This will result in a function $\mathscr{E}_{rms}$ versus D, the minimum of which will then give the best-estimate value of D.

Figures 5(a) and 5(b) show the functions $\mathscr{E}_{rms}(D)$ which are calculated from the measurement data at λ=400 and 750 nm, respectively. In the case of λ=400 nm, where $k\neq 0$, $\mathscr{E}_{rms}$ changes only slightly with D. For example, $\mathscr{E}_{rms}$ decreases from 0.423° at $D=100$ nm to its minimum value of 0.410° at $D=112$ nm; the change is only 0.13°. Our measurement resolution is about 0.005°, which is roughly estimated as follows: since there are 90 measured data points of θ and ϵ, and the error of the measurements is smaller than 0.05°, the rms error should be about $0.05/\sqrt{90} \simeq 0.005°$. With this resolution applied to Fig. 5(a), the error in the estimated D should be less than ±2 nm. In the case of λ=750 nm, we found $k\simeq 0.00$, and therefore,

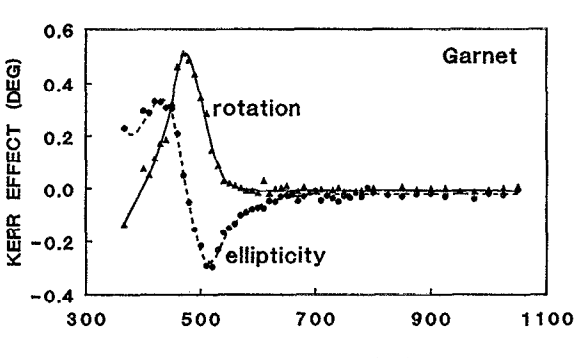

FIG. 10. Measured θ_k and ϵ_k of the BiFe garnet sample vs λ. The probe beam was incident on the film side, and the bottom side of the substrate was covered with black tape.

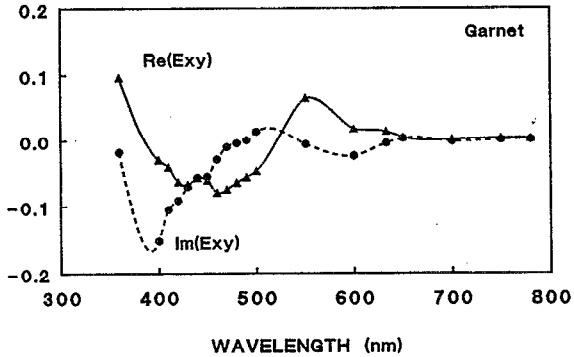

FIG. 11. Best-estimate values of $\mathrm{Re}(\epsilon_{xy})$ and $\mathrm{Im}(\epsilon_{xy})$ vs λ for the BiFe garnet.

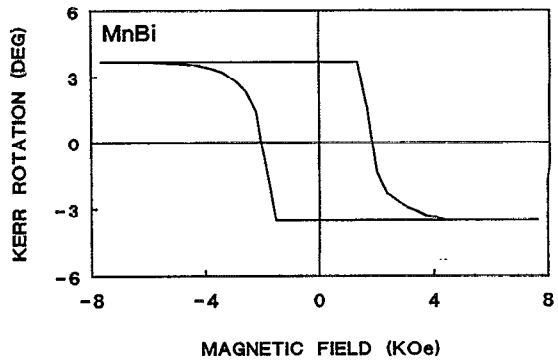

FIG. 13. Kerr hysteresis loop for the MnBi sample as measured from the film side at λ=633 nm.

$\mathscr{E}_{\mathrm{rms}}$ depends sensitively on D. The best-estimate thickness in this case is $D=113$ nm, which agrees quite well with that obtained at λ=400 nm.

Figures 6(a) and 6(b) show the experimental data of θ and ϵ (circles) measured at λ=750 nm, the best theoretical fit calculated using $D=113$ nm (solid curves), and the fit obtained with adjustable n and k, but with D fixed at its nominal value of 100 nm (dashed curves). Evidently, the best-estimate value of D gives substantially better fit to the measured ϵ than does the nominal thickness.

The estimated values of D at other wavelengths are: D=97 (λ=450 nm), 110 (λ=500 nm), 95 (λ=550 nm), 104 (λ=600 nm), 105 (λ=633 nm), 103 (λ=650 nm), 112 (λ=700 nm), and 113 nm (λ=780 nm). [These values could be reproduced within ± 1 nm by repeating the measurements.] In the case of λ=450 nm, the measured ϵ is close to zero for all Θ_{inc} (because the phase effect of the absorption on the reflected beam cancels that caused by reflection from the interface), so that the information is not sufficient for a good estimate of D. For λ=550, 600, 633, and 650 nm, we found it very hard to make a clear distinction while measuring θ and ϵ. This indicates that the polarization state over the cross section of the reflected beam is not uniform, from which we might conclude that the optical properties at different locations of the film are not the same (at Θ_{inc}=60° the spot size of the beam at the sample surface is about 1×5 mm^2). This nonuniformity seems to have the strongest effect on the reflected polarization state when destructive interference occurs (in the valley of the reflectance curve in Fig. 4). Based on these considerations, we believe that the measurement data at λ=400, 500, 700, 750, and 780 nm give better estimates of D, and, therefore, choose D=113 nm as the best estimate of thickness for the BiFe garnet film. Having fixed the thickness, the values of n and k can be readily estimated

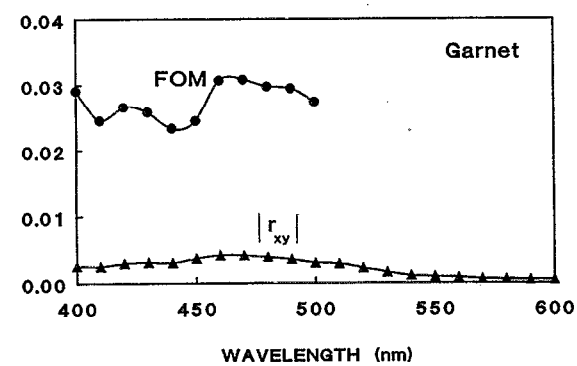

FIG. 12. Measured $|r_{xy}|$ and computed FOM vs λ for the BiFE garnet sample. [For $\lambda \geqslant 550$ nm, the absorption coefficient k drops to zero, and the expression for the FOM in Eq. (3) becomes inapplicable.]

TABLE II. Best-estimate values of refractive indices, dielectric tensor elements, and thicknesses for the sample of SiO/MnBi/glass substrate.

Layer Material Thickness Wavelength (nm)	Layer 1 SiO 237 nm		Layer 2 MnBi 50 nm				Substrate Glass 0.21 mm
	n	k	n	k	ϵ_{xx}	ϵ_{xy}	n
360	2.062	0.257	1.179	1.740	−1.64 +i4.10	−0.288 −i0.217	1.537
400	2.006	0.130	1.475	2.251	−2.89 +i6.64	−0.439 −i0.228	1.531
450	1.989	0.034	2.100	2.487	−1.78 +i10.44	−0.552 −i0.186	1.525
500	1.937	0.018	2.516	2.554	−0.19 +i12.85	−0.680 −i0.128	1.521
550	1.905	0.015	2.649	2.541	0.56 +i13.46	−0.876 −i0.071	1.519
600	1.885	0.000	2.734	2.730	0.02 +i14.93	−1.137 +i0.003	1.516
633	1.835	0.000	2.725	2.585	0.74 +i14.09	−1.332 +i0.091	1.515
650	1.835	0.002	2.721	2.617	0.56 +i14.24	−1.409 +i0.145	1.515
700	1.825	0.000	2.745	2.757	−0.07 +i15.13	−1.581 +i0.443	1.513
750	1.831	0.000	2.964	2.916	0.29 +i17.28	−1.489 +i1.017	1.512
780	1.840	0.000	3.271	2.965	1.91 +i19.40	−1.218 +i1.557	1.511
820	1.861	0.000	3.874	2.659	7.94 +i20.60	−0.490 +i2.588	1.511
830	1.876	0.000	4.080	2.627	9.75 +i21.44	−0.226 +i2.912	1.510
840	1.884	0.000	4.277	2.509	12.00 +i21.46	0.075 +i3.266	1.510
860	1.885	0.000	4.301	2.533	12.08 +i21.79	0.801 +i3.667	1.510

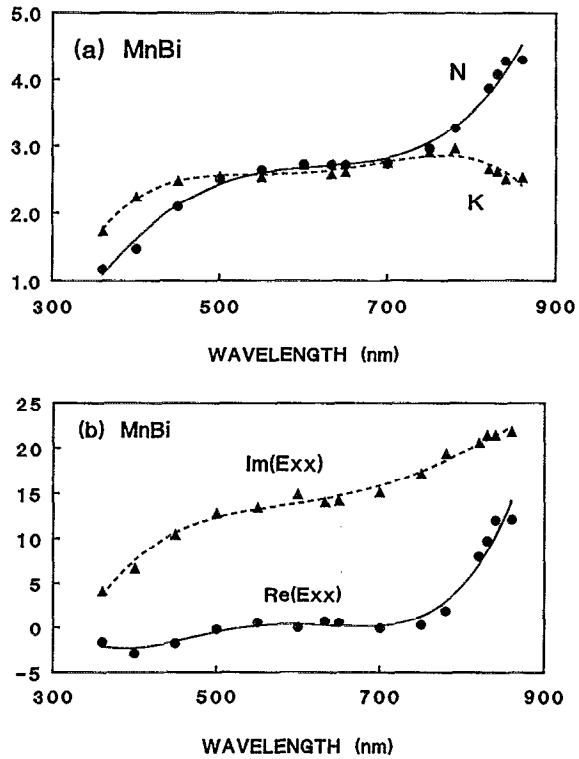

FIG. 14. Plots of the best-estimate values of (a) n and k, and (b) $\mathrm{Re}(\epsilon_{xx})$ and $\mathrm{Im}(\epsilon_{xx})$ for the MnBi layer vs λ.

by matching the measurement data at λ with theoretical calculations. Figures 7(a) and 7(b) show the best-estimate values of n, k, and ϵ_{xx} versus λ.

To know the accuracy of the estimated parameters, we studied how the fitting quality changes if one of the parameters deviates from its best-estimate value by a certain percentage. We chose the measurement data of θ and ϵ versus Θ_{inc} at $\lambda=500$ nm for this consideration. The parameters that give the best fit to the measured data are $(n, k, D)=(2.631, 0.164, 113\ \mathrm{nm})$. We calculated θ and ϵ for the following three sets of parameters: $(n, k, D)=(2.60, 0.164, 113\ \mathrm{nm})$, i.e., n is 1% off, $(2.631, 0.156, 113\ \mathrm{nm})$, i.e., k is 5% off, and $(2.631, 0.164, 110\ \mathrm{nm})$, i.e., D is 3% off. To display the results on a suitable scale, we plot the mismatch between the

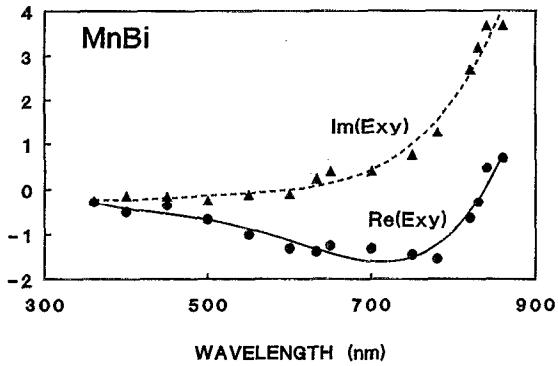

FIG. 16. Best-estimate values of $\mathrm{Re}(\epsilon_{xy})$ and $\mathrm{Im}(\epsilon_{xy})$ for the MnBi sample vs λ.

calculated (θ, ϵ) and the measured data versus Θ_{inc} in Figs. 8(a) and 8(b). In these figures, the solid curve corresponds to the best fit, while the remaining three curves are obtained using one of the above sets of parameters. Since our measurement errors for θ and ϵ are smaller than the calculated mismatch, the errors in the best-estimate parameters should be smaller than the deviations chosen for these calculations. We thus estimate that, in this particular case, the error for the best-estimate value of n is less than 0.5%, for k it is <2%, and for D it is <1%.

To examine whether the MO Kerr effect has any influence on the n and k measurements, we measured θ and ϵ for both up and down states of magnetization of the sample at $\lambda=500$ nm, where the sample shows large θ_k and ϵ_k. The measured values of ϵ are shown in Fig. 9. We found $(n, k, D)=(2.631, 0.165, 110\ \mathrm{nm})$ for up magnetization, and $(2.627, 0.174, 111\ \mathrm{nm})$ for down magnetization. The difference would become smaller at other wavelengths because θ_k and ϵ_k will be smaller. These results show that, to a good approximation, the Kerr effect is negligible in the measurement of n, k, and D.

We also checked for the presence of optical anisotropy in the sample by measuring θ and ϵ versus Θ_{inc} for $\lambda=650$ nm at two different azimuthal angles of incidence, $\Phi_{\mathrm{inc}}=0°$ and $\Phi_{\mathrm{inc}}=90°$. The measured values in these two cases were identical within measurement accuracy, indicating that the optical anisotropy, if any, should be negligible.

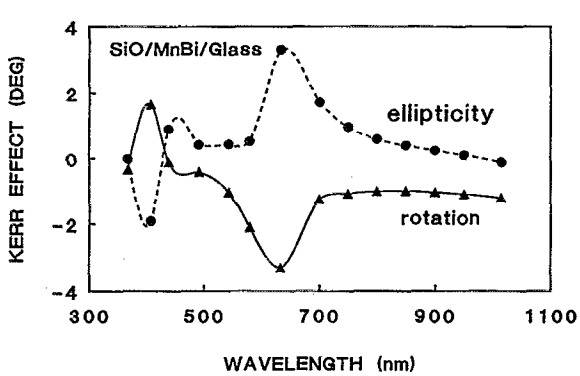

FIG. 15. Measured θ_k and ϵ_k vs λ for the SiO/MnBi/glass sample. Measurements were performed from the film side.

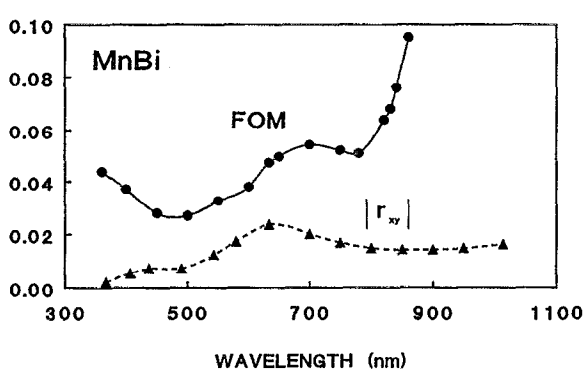

FIG. 17. Measured $|r_{xy}|$ for the SiO/MnBi/glass sample and the calculated FOM for the MnBi material of this sample vs λ.

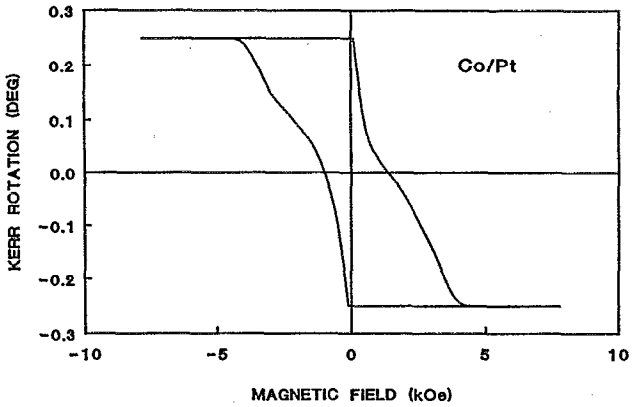

FIG. 18. Kerr hysteresis loop for the Co/Pt sample as measured from the film side at $\lambda=633$ nm.

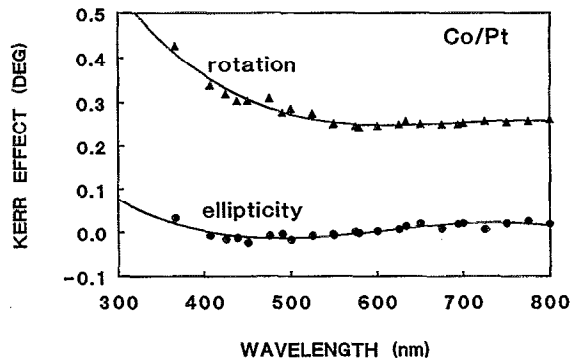

FIG. 20. Measured θ_k and ϵ_k vs λ for the Co/Pt sample. The probe beam was incident on the film side.

Having determined the thickness D and the diagonal element ϵ_{xx}, calculation of the off-diagonal element ϵ_{xy} turns out to be fairly straightforward. Figure 10 shows plots of the Kerr rotation angle θ_k and ellipticity ϵ_k versus wavelength, as measured from the film side of the sample. Figure 11 shows the estimated ϵ_{xy} versus λ. The best-estimate values of all parameters for this sample are listed in Table I. Figure 12 shows plots of the calculated FOM for the bismuth-substituted garnet material and $|r_{xy}|$ for the particular sample studied here.

B. MnBi

Thin films of MnBi are attractive for MO recording because of this material's large Kerr rotation angle and strong perpendicular magnetic anisotropy.[14–17] However, the grain boundary noise, and the structural phase transition occurring after repeated write-erase cycles pose serious problems for the application of this material in MO recording. Recently, research has indicated that these problems may be resolved if MnBi films were doped with an appropriate third element such as aluminum.[18–20] This development has rekindled interest in MnBi-based alloys as potential candidate materials for high density recording media.

Our sample consists of a MnBi layer deposited onto a glass substrate and overcoated with a SiO layer. The nominal thickness of MnBi is 50 nm, and that of the SiO overcoat about 200 nm. This sample has perpendicular magnetic anisotropy and a fairly square hysteresis loop with $H_c \simeq 2$ kOe as may be seen in Fig. 13.

We measured θ and ϵ versus $\Theta_{\rm inc}$ at different wavelengths, and derived the thickness and ordinary optical constants for the SiO layer and the MnBi layer simultaneously from the measurement data. Since the MnBi layer was fairly thick, the fitting quality and the values of n and k do not depend sensitively on the thickness of this layer, the nominal thickness of 50 nm was used in the data analyses. The best-estimate parameters are given in Table II. The best-estimate values of n and k, and also ϵ_{xx} for the MnBi film are plotted in Fig. 14.

The measured Kerr rotation θ_k and ellipticity ϵ_k for the SiO/MnBi/glass sample are plotted in Fig. 15. These mea-

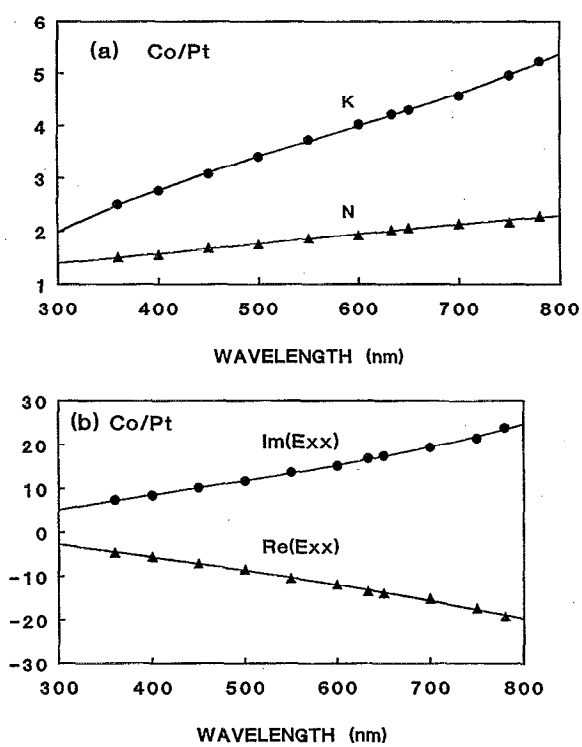

FIG. 19. Best-estimate values of (a) n and k, and (b) $\mathrm{Re}(\epsilon_{xx})$ and $\mathrm{Im}(\epsilon_{xx})$ vs λ for the Co/Pt sample.

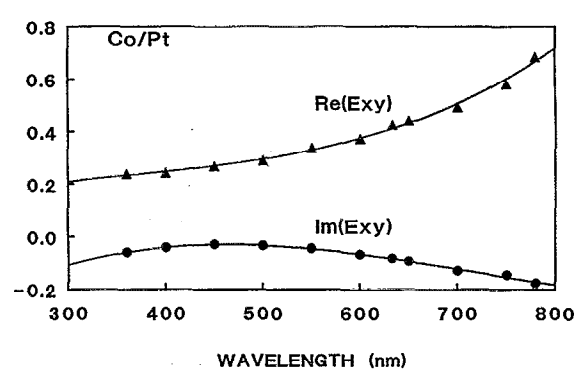

FIG. 21. Best-estimate values of $\mathrm{Re}(\epsilon_{xy})$ and $\mathrm{Im}(\epsilon_{xy})$ vs λ for the Co/Pt sample.

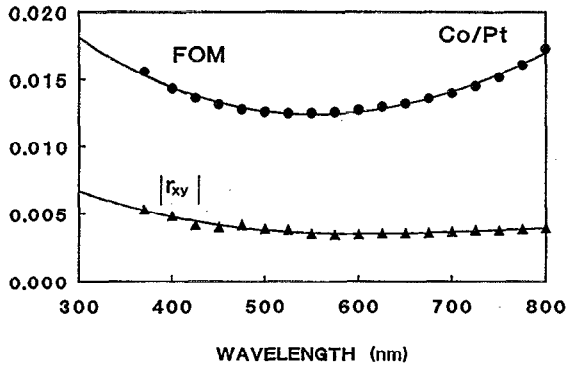

FIG. 22. Measured $|r_{xy}|$ and the computed FOM for the Co/Pt sample vs λ.

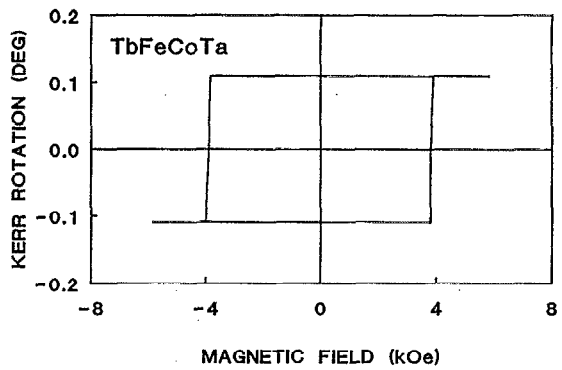

FIG. 23. Kerr hysteresis loop of the TbFeCoTa sample as measured from the film side at λ=633 nm.

surements were done with the beam incident on the SiO side of the sample. The derived off-diagonal dielectric constant ϵ_{xy} is plotted versus λ in Fig. 16. The measured $|r_{xy}|$ for this sample and the calculated FOM for MnBi are plotted in Fig. 17. The numerical values of the various parameters are also listed in Table II.

C. Co/Pt multilayer

Since Carcia *et al.* showed that the Co/Pd multilayers possess perpendicular magnetic anisotropy and large Kerr rotation at short wavelengths,[21] a vast amount of research work has been devoted to multilayered thin films such as Co/Pd, Co/Pt, Fe/Pt, etc.[22–26] The Co/Pt multilayers turn out to be most promising for high density recording. Among many factors, the properties of Co/Pt multilayers depend sensitively on the layer structure. One of the best layer structures consists of 3-Å-thick cobalt and 4-Å-thick platinum layers.

Our Co(3 Å)/Pt(4 Å) sample has 43 bilayers, is sputter-deposited on glass substrate, and has no overcoat. The nominal film thickness is 301 Å, the sample has perpendicular magnetic anisotropy, and its hysteresis loop is square with $H_c=1.9$ kOe, as shown in Fig. 18. The transmittance of the sample is essentially zero at all wavelengths, indicating that the film is thick enough that no light reaches the film–substrate interface. Therefore, we set $D=30$ nm. Figure 19 shows the best-estimate values of n and k, and also the values of ϵ_{xx}. Figure 20 shows the measured θ_k and ϵ_k, and Fig. 21 shows the best-estimate values of ϵ_{xy}. Figure 22 shows the calculated FOM for this particular composition of

TABLE III. Best-estimate values of refractive indices and dielectric tensor elements for the sample of Co/Pt multilayer with glass substrate.

Layer material thickness Wavelength (nm)	Layer 1 Co(3 Å)/Pt(4 Å)×43 30 nm				Substrate Glass 1.21 mm
	n	k	ϵ_{xx}	ϵ_{xy}	n
360	1.443	2.573	−4.54 +i7.42	0.239 −i0.059	1.537
400	1.515	2.787	−5.47 +i8.44	0.243 −i0.040	1.531
450	1.638	3.114	−7.01 +i10.20	0.268 −i0.029	1.525
500	1.739	3.381	−8.40 +i11.76	0.289 −i0.034	1.521
550	1.851	3.726	−10.45 +i13.79	0.339 −i0.044	1.519
600	1.931	3.956	−11.92 +i15.28	0.372 −i0.067	1.516
633	2.018	4.195	−13.52 +i16.93	0.427 −i0.083	1.515
650	2.057	4.261	−13.92 +i17.53	0.442 −i0.093	1.514
700	2.180	4.458	−15.12 +i19.44	0.495 −i0.13	1.513
750	2.273	4.739	−17.29 +i21.54	0.582 −i0.15	1.512
780	2.395	4.995	−19.21 +i23.92	0.685 −i0.18	1.511

TABLE IV. Best-estimate values of refractive indices, dielectric tensor elements, and thickness for the sample of SiC/TbFeCoTa/SiC/glass substrate.

Layer material thickness Wavelength (nm)	Layer 1,3 SiC 13 nm		Layer 2 TbFeCoTa 14 nm				Substrate Glass 0.95 mm
	n	k	n	k	ϵ_{xx}	ϵ_{xy}	n
400	2.903	0.624	2.334	3.451	−6.46 +i16.11	−0.185 +i0.233	1.515
450	2.919	0.491	2.533	3.665	−7.02 +i18.57	−0.226 +i0.268	1.508
500	2.884	0.398	2.728	3.862	−7.47 +i21.07	−0.336 +i0.281	1.504
550	2.862	0.323	2.920	4.041	−7.80 i23.60	−0.435 +i0.242	1.502
600	2.844	0.259	3.110	4.203	−7.99 +i26.14	−0.545 +i0.201	1.500
633	2.834	0.231	3.203	4.277	−8.03 +i27.40	−0.602 +i0.200	1.499
650	2.824	0.206	3.296	4.347	−8.03 +i28.66	−0.670 +i0.160	1.499
700	2.800	0.165	3.480	4.473	−7.90 +i31.13	−0.763 +i0.129	1.499
750	2.772	0.135	3.661	4.582	−7.59 +i33.54	−0.867 +i0.053	1.499
780	2.758	0.125	3.750	4.630	−7.37 +i34.72	−0.925 +i0.037	1.499

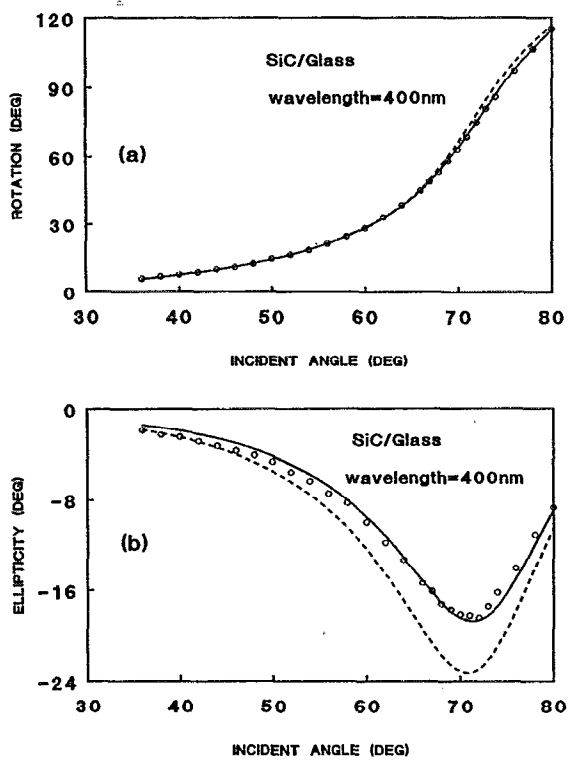

FIG. 24. Comparison between the ellipsometry results and those obtained with the reflection-transmission technique. The measured data (circles) of θ (a) and ϵ (b) were taken at $\lambda=400$ nm and $\Psi_{pol}=20°$. The solid curves are the best fits to the measured data which give $(n, k)=(2.914, 0.630)$. The dashed curves are calculated with $(n, k)=2.918, 0.483)$ as given by the reflection-transmission technique.

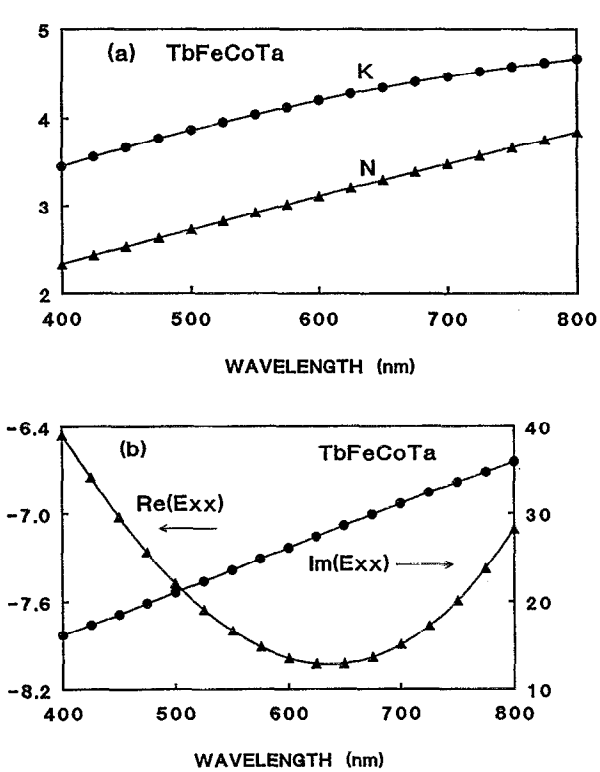

FIG. 25. Best-estimate values of (a) n and k, and (b) $\mathrm{Re}(\epsilon_{xx})$ and $\mathrm{Im}(\epsilon_{xx})$ vs λ for the TbFeCoTa layer.

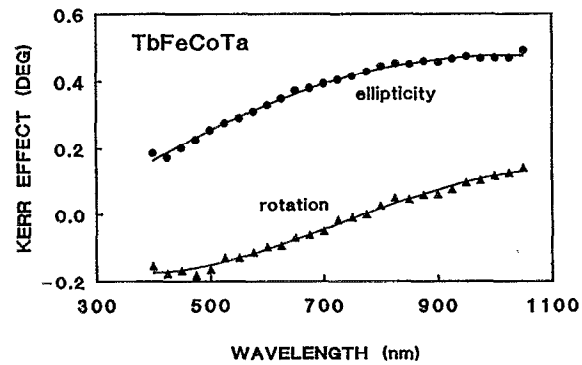

FIG. 26. Measured θ_k and ϵ_k vs λ for the SiC/TbFeCoTa/SiC/glass sample. The probe beam was incident on the film side of the sample.

Co/Pt, and the measured $|r_{xy}|$ versus λ for the sample under investigation. The values of the various parameters are also listed in Table III.

D. TbFeCoTa

Amorphous TbFeCo films are presently the media of choice for red and infrared MO recording. The Kerr effect of TbFeCo, however, decreases at short wavelengths. Some recent studies have indicated that the TbFeCo disk noise is smaller than that of Co/Pt multilayers at short wavelength ($\lambda=532$ nm), and its carrier-to-noise ratio (CNR) therefore remains at the level of the Co/Pt disk.[27] It is thus conceivable that future generations of MO media will continue to use TbFeCo as their basic material, although some other elements may have to be added to improve the properties in the blue–green regime of wavelengths. We present our measurement results on a TbFCoTa sample that is used by at least one manufacturer of MO disks. These results also serve as a reference for comparing with other types of media considered in this paper.

Our sample has a trilayer structure as follows: SiC(130 Å)/TbeFeCoTa(140 Å)/SiC(130 Å)/glass substrate; the nominal thicknesses are indicated in parentheses. In order to reduce the number of unknowns, a second sample, consisting of SiC(130 Å) on glass substrate, was prepared under the same conditions, and was separately characterized. Figure 23 shows the Kerr hysteresis loop for the TbFeCoTa sample

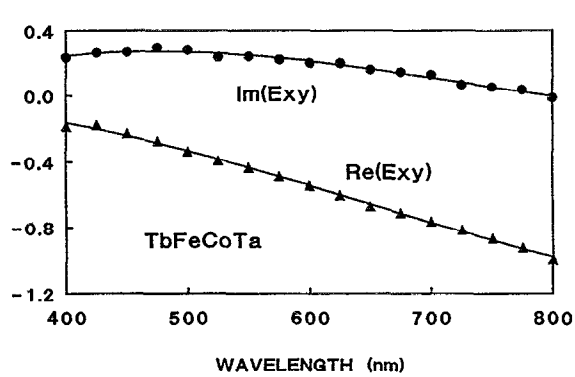

FIG. 27. Best-estimate values of $\mathrm{Re}(\epsilon_{xy})$ and $\mathrm{Im}(\epsilon_{xy})$ vs λ for the TbFeCoTa layer.

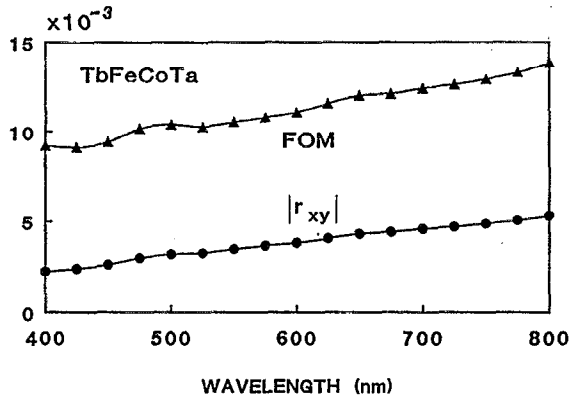

FIG. 28. Measured $|r_{xy}|$ for the SiC/TbFeCoTa/SiC/glass sample and the computed FOM for the TbFeCoTa material vs λ.

measured at λ=633 nm. We cut one piece from the SiC/glass sample, and removed the SiC layer from it by ion milling in order to obtain the bare glass substrate. We first measured the refractive index n of the bare substrate using the method described in Sec. III A. The measured T of the bare substrate agrees with the Fresnel formula for a nonabsorbing medium, $T=16\,n^2\,(1+n)^4$, within 2% error. We have thus concluded that the absorption of the substrate is negligible ($k\leqslant 10^{-6}$) in the wavelength range of interest.

Next, we measured the data sets 1, 2, and 3 for the SiC/glass sample, and searched for the best match. Good match could be achieved within the range of 130 Å$\leqslant D\leqslant$150 Å, and we fixed D as its nominal value of 130 Å. The best-estimate values of n and k of the SiC layer are given in Table IV. We compared these results with those obtained by the reflection-transmission technique, in which the n and k are calculated from R and T measured at normal incidence. For example, at λ=400 nm, the ellipsometric technique gives $n=2.914$, $k=0.630$, while the reflection-transmission technique gives $n=2.918$, $k=0.483$. (The same thickness of 13 nm was used in both analyses.) Figures 24(a) and 24(b) show the measured (θ, ϵ) and the calculated values using the two sets of n and k. Within the measurement accuracy, both sets of parameters are seen to give good match to the measured data at small $\Theta_{\rm inc}$, but at larger $\Theta_{\rm inc}$, the ellipsometric method gives a better match. Once again, this emphasizes the importance of measuring θ and ϵ in a wide range of $\Theta_{\rm inc}$. The best-estimate values (n, k, D) for the SiC layer thus obtained will be used to describe the overcoat and the underlayer in the data analysis for the sample containing the TbFeCoTa layer.

Finally, we measured the four sets of data for the SiC TbFeCoTa/SiC/glass sample. Having determined (n, k, D) for the SiC layer, we only searched for (n, k, D) of the TbFeCoTa layer to match the measured data. Since good match could be obtained with 120 Å$\leqslant D\leqslant$140 Å for the magnetic layer, we adopted the nominal value of $D=140$ Å.

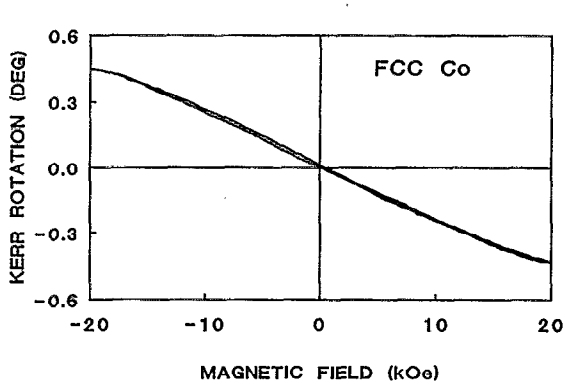

FIG. 29. Kerr rotation angle vs the perpendicularly applied magnetic field for the sample of fcc cobalt. This sample has in-plane magnetization, and the field required to bring it into the perpendicular direction is just over 20 kOe.

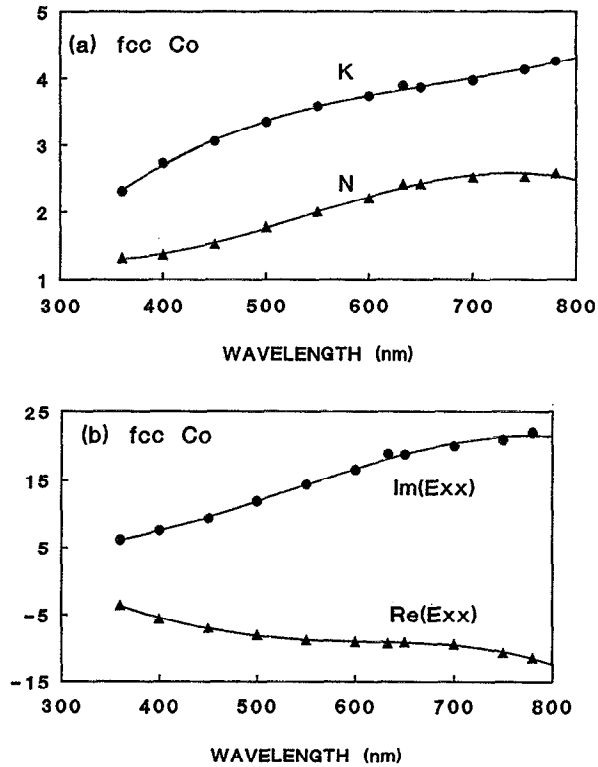

FIG. 30. Best-estimate values of (a) n and k, and (b) Re(ϵ_{xx}) and Im(ϵ_{xx}) vs λ for the fcc cobalt film.

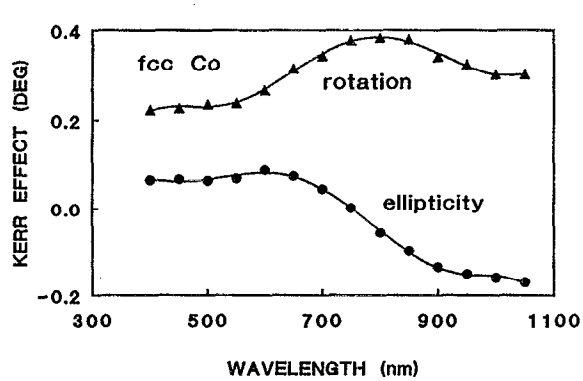

FIG. 31. Measured θ_k and ϵ_k vs λ for the fcc cobalt sample. Since the magnetization of this sample is in-plane, a 14 kOe magnetic field was applied in the perpendicular direction of the sample, which produced a perpendicular component of magnetization to allow the Kerr effect measurements.

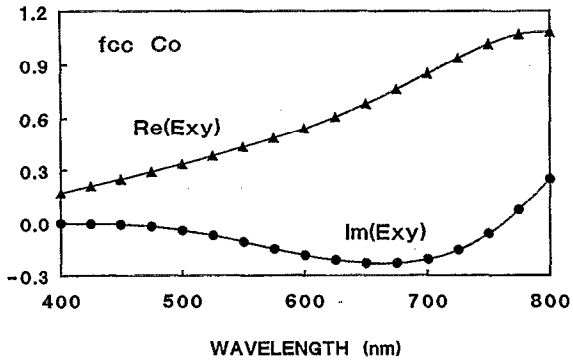

FIG. 32. Best-estimate values of $\mathrm{Re}(\epsilon_{xy})$ and $\mathrm{Im}(\epsilon_{xy})$ vs λ for the fcc cobalt.

The best-estimate values of n, k, ϵ_{xx}, the measured data of θ_k and ϵ_k, the best-estimate values of ϵ_{xy}, the measured $|r_{xy}|$, and the calculated FOM are shown in Figs. 25–28, respectively. The numerical values of the various parameters are also listed in Table IV.

E. Thin film of crystalline fcc cobalt

Under normal conditions cobalt has hcp structure at room temperature. It has been found recently, however, that crystalline films of cobalt with fcc structure can be grown on appropriate substrates. These films exhibit a larger MO effect than ordinary cobalt films. Our fcc Co sample has the layer structure Co(500 Å)/Cu(1000 Å)/Si substrate. The sample has in-plane magnetization and its saturation field (the minimum field required to bring the magnetization into perpendicular orientation) is about 20 kOe (see Fig. 29).

We measured data sets 1, 2, and 4 for this sample. In matching the data, we took n and k of Cu layer from the literature.[28] The exact values for our sample may slightly differ from the published values, but the Cu layer should have a very small effect on the measurements because the Co layer is fairly thick. The best-estimate values of n, k, ϵ_{xx}, the measured data of θ_k and ϵ_k, the best-estimate values of ϵ_{xy}, the measured $|r_{xy}|$, and the calculated FOM are shown in Figs. 30–33, respectively. Notice that θ_k and ϵ_k shown in Fig. 31 were measured under the applied field of 14 kOe (maximum available field in our MOKS system). The Kerr

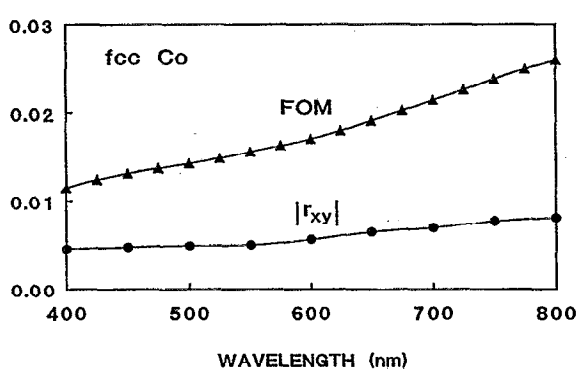

FIG. 33. Measured $|r_{xy}|$ for the sample of fcc Co/Cu/Si-substrate sample and the computed FOM for the fcc cobalt vs λ.

TABLE V. Best-estimate values of refractive indices and dielectric tensor elements for the sample of the Co (fcc)/Cu/Si substrate. The n and k data for the Cu layer were taken from Ref. 28.

Layer material thickness Wavelength (nm)	Layer 1 Co(fcc) 50 nm				Layer 2 Cu 100 nm	
	n	k	ϵ_{xx}	ϵ_{xy}	n	k
400	1.389	2.703	−5.38 +i7.51	0.173 −i0.001	1.204	2.125
450	1.551	3.077	−7.07 +i9.55	0.251 −i0.008	1.161	2.396
500	1.765	3.362	−8.19 +i11.87	0.337 −i0.041	1.149	2.571
550	2.001	3.578	−8.80 +i14.32	0.435 −i0.107	0.966	2.588
600	2.230	3.744	−9.04 +i16.70	0.541 −i0.183	0.386	2.940
633	2.370	3.841	−9.14 +i18.21	0.607 −i0.210	0.234	3.430
650	2.422	3.881	−9.19 +i18.80	0.682 −i0.227	0.219	3.616
700	2.547	4.008	−9.58 +i20.42	0.853 −i0.204	0.211	4.146
750	2.576	4.147	−10.56 +i21.37	1.018 −i0.060	0.234	4.613
780	2.535	4.244	−11.58 +i21.52	1.074 +i0.074	0.275	4.889

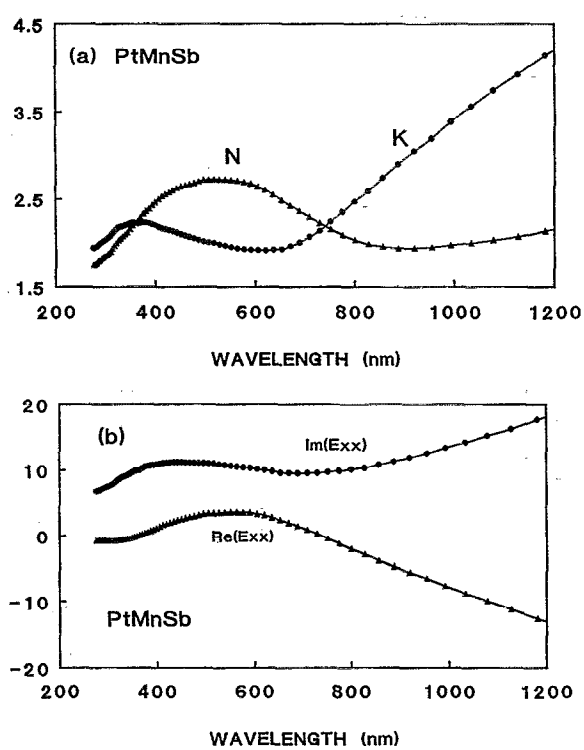

FIG. 34. Best-estimate values of (a) n and k, and (b) $\mathrm{Re}(\epsilon_{xx})$ and $\mathrm{Im}(\epsilon_{xx})$ vs λ for the Heusler alloy PtMnSb (Ref. 30).

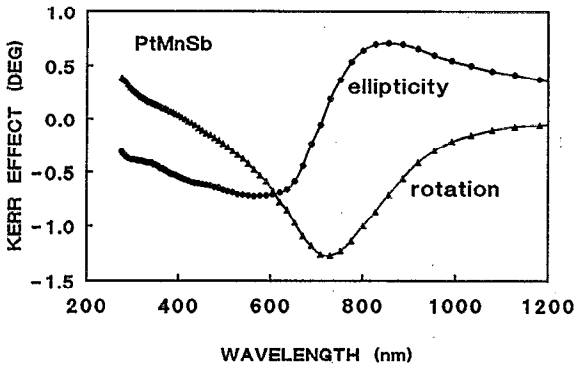

FIG. 35. Measured θ_k and ϵ_k vs λ for the Heusler alloy PtMnSb (Ref. 30).

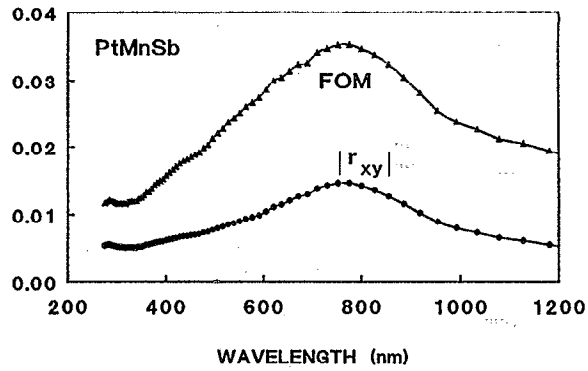

FIG. 37. Off-diagonal reflectivity $|r_{xy}|$ as measured from the polished surface of the bulk Heusler alloy PtMnSb, and the computed FOM for this material vs λ.

rotation angle and ellipticity that would have been obtained under the saturation field, $\theta_k^{\rm sat}$ and $\epsilon_k^{\rm sat}$, can be found by multiplying the measured data with a factor of 20/14, i.e., $\theta_k^{\rm sat} = 1.43\ \theta_k$ and $\epsilon_k^{\rm sat} = 1.43\ \epsilon_k$. The values of $\theta_k^{\rm sat}$ and $\epsilon_k^{\rm sat}$ have been used in the calculation of ϵ_{xy}. Table V lists the numerical values of the various parameters.

F. The Heusler alloy PtMnSb

The Heusler alloy PtMnSb is another material with appreciable Kerr effect. We collected from the literature the data of ϵ_{xx}, θ_k, and ϵ_k as measured from the polished surfaces of bulk PtMnSb alloy.[29,30] We then calculated ϵ_{xy} using the formula and, from there, calculated FOM and $|r_{xy}|$. The results are plotted in Figs. 34–37:

$$\theta_k - i\epsilon_k = \frac{\epsilon_{xy}}{\sqrt{\epsilon_{xx}(1-\epsilon_{xx})}}. \tag{9}$$

IV. SUMMARY

We have established a dielectric tensor database for thin film media of interest in high density MO recording. Our measurement method involves a combination of variable angle ellipsometry, reflection-transmission measurements, and polar Kerr effect measurements. The MULTILAYER program has been employed to analyze the measurement data and search for the best-estimate values of the unknown parameters. This method, which comprises measurements at a wide range of incident angles and at different wavelengths, provides a high degree of accuracy for characterizing the thickness and the dielectric tensor elements of thin film samples.

In order to achieve the highest degree of accuracy, we have measured separately the bare substrate for samples with a thin MO layer. Different aspects of the measurements, such as the accuracy of the best-estimate parameters, the influence of the Kerr effect on the measurement of the diagonal element, the effect of optical anisotropy, and the differences between the ellipsometric technique and the reflection-transmission technique have been investigated in order to ensure the validity of the results.

We have obtained the wavelength dependence of the dielectric tensor for the following MO materials: $(BiDy)_3(FeGa)_5O_{12}$, MnBi, multilayered Co/Pt, TbFeCoTa, and fcc cobalt. We have also summarized the measurement results for the Heusler alloy PtMnSb, which has been available from the literature. In the blue–green regime of 400 nm$\leqslant\lambda\leqslant$550 nm, the relationship among the derived values of FOM for these materials is as follows: $\mathrm{FOM}_{\rm MnBi}$ ($\approx$0.027–0.045)$\approx\mathrm{FOM}_{\rm Garnet}$ ($\approx$0.023–0.032)$>\mathrm{FOM}_{\rm PtMnSb}$ ($\approx$0.015–0.026)$>\mathrm{FOM}_{\rm Co/Pt}$ ($\approx$0.013–0.015)$\approx\mathrm{FOM}_{\rm Co(fcc)}$ ($\approx$0.011–0.016)$>\mathrm{FOM}_{\rm TbFeCoTa}$ ($\approx$0.009–0.011).

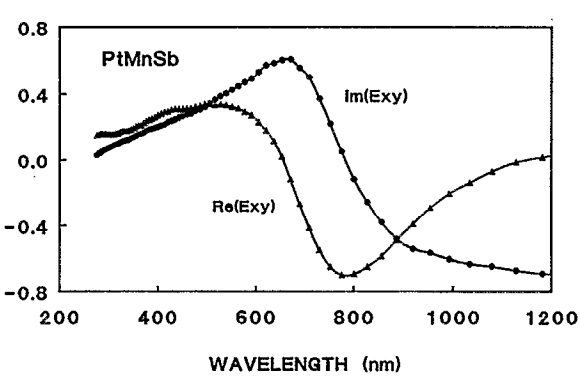

FIG. 36. Best-estimate values of $\mathrm{Re}(\epsilon_{xy})$ and $\mathrm{Im}(\epsilon_{xy})$ vs λ for the Heusler alloy PtMnSb (Refs. 29 and 30).

ACKNOWLEDGMENTS

The idea of establishing a dielectric tensor database for materials of interest for high density MO recording came from Dr. R. Victora of Eastman Kodak Company. We are grateful to Dr. T. Suzuki of the IBM Almaden Research Center, Dr. Di Chen of Chen and Associates Consulting, Dr. D. Sellmeyer, Dr. R. D. Kirby, and Dr. J. Chen of the University of Nebraska at Lincoln, Dr. P. Carcia of the DuPont Corporation, and Dr. W. Challener of the 3M Company who provided the samples for this study. Thanks are also due to Professor M. Ruane of Boston University for his help in developing the control program for the MOKS system, and to Mr. I. Syrgabaev for the measurement of the Kerr hysteresis loops. This work has been supported by a grant from the Advanced Research Projects Agency (ARPA) under a contract (Contract No. MDA 972-93-1-0009) with the National

Storage Industries Consortium (NISC), and in part by the Optical Data Storage Center (ODSC) at the University of Arizona.

[1] M. Mansuripur, Appl. Phys. Lett. **49**, 19 (1986).
[2] M. Mansuripur, *The Physical Principles of Magneto-Optical Recording* (Cambridge University, London, 1994).
[3] G. A. N. Connell, Appl. Opt. **22**, 3155 (1983).
[4] M. Ruane, M. Mansuripur, and R. Rosenvold, Appl. Opt. **25**, 1946 (1986).
[5] A. F. Zhou, J. K. Erwin, C. F. Brucker, and M. Mansuripur, Appl. Opt. **31**, 6280 (1992).
[6] M. Mansuripur, J. Appl. Phys. **67**, 6466 (1990).
[7] F. L. McCrackin, E. Passaglia, R. R. Stromberg, and H. L. Steinberg, J. Res. Natl. Bur. Stand. A **67**, 363 (1963).
[8] M. Mansuripur, A. F. Zhou, and J. K. Erwin, Appl. Opt. **29**, 1308 (1990).
[9] A. F. Zhou, Ph.D thesis, University of Arizona, 1992.
[10] R. A. Hajjar, Ph.D thesis, University of Arizona, 1992.
[11] K. Shono, H. Kano, N. Konishi, and S. Ogawa, J. Appl. Phys. **63**, 3639 (1988).
[12] T. Suzuki, F. Sequeda, H. Do, T. C. Huang, and G. Gorman, J. Appl. Phys. **67**, 4435 (1990).
[13] P. A. Crozier, P. A. Labun, and T. Suzuki, J. Magn. Soc. Jpn. **17**, Suppl. S1, 241 (1993).
[14] D. Chen, J. F. Ready, and E. Bernal G., J. Appl. Phys. **39**, 3916 (1968).
[15] D. Chen and R. L. Aagard, J. Appl. Phys. **41**, 2530 (1970).
[16] E. Feldtkeller, IEEE Trans. Magn. **MAG-8**, 481 (1972).
[17] D. Chen, G. N. Otto, and F. M. Schmit, IEEE Trans. Magn. **MAG-9**, 66 (1973).
[18] Y. J. Wang, J. Magn. Magn. Mater. **84**, 39 (1990).
[19] J. X. Shen, R. D. Kirby, D. J. Sellmyer, and Y. J. Wang, J. Appl. Phys. **69**, 5984 (1991).
[20] Y. J. Wang, C. P. Luo, L. C. Kong, X. S. Qi, D. Huang, and Y. Chen, J. Magn. Soc. Jpn. **17**, Suppl. S1, 294 (1993).
[21] P. F. Carcia, A. D. Meinhaldt, and A. Suna, Appl. Phys. Lett. **47**, 178 (1985).
[22] P. F. Carcia, J. Appl. Phys. **63**, 5066 (1988).
[23] W. B. Zeper, F. J. A. M. Greidanus, P. F. Carcia, and C. R. Fincher, J. Appl. Phys. **65**, 4971 (1989).
[24] S. Hashimoto and Y. Ochiai, J. Magn. Magn. Mater. **88**, 211 (1990).
[25] T. Suzuki, H. Notarys, S. S. Parkin, S. Iwata, and D. Dobbertin, SPIE Proc. **1663**, 257 (1992).
[26] K. Sato, J. Magn. Soc. Jpn. **17**, Suppl. S1, 11 (1993).
[27] M. Takahashi, J. Nakamura, M. Ojima, and K. Tatsuno, SPIE Proc. **1663**, 250 (1992).
[28] *CRC Handbook of Chemistry and Physics*, edited by R. C. Weast, D. R. Lide, M. J. Astle, and W. H. Beyer (Chemical Rubber, Boca Raton, FL, 1989), Chap. 6.
[29] P. G. van Engen, K. H. J. Buschow, and R. Jongebreur, Appl. Phys. Lett. **42**, 202 (1983).
[30] P. A. M. van der Heide, W. Baelde, R. A. de Groot, A. R. de Vroomen, P. G. van Engen, and K. H. J. Buschow, J. Phys. F **15**, L75 (1985).